

Information-Theoretic Active Contour Model for Microscopy Image Segmentation Using Texture

Veronica Biga¹(✉) and Daniel Coca²

¹ Faculty of Biology, Medicine and Health, The University of Manchester,
Oxford Rd, M13 9PL Manchester, UK

`veronica.bigamanchester.ac.uk`

² Department of Automatic Control and Systems Engineering,
The University of Sheffield, Mappin Street, S1 3JD Sheffield, UK
`d.coca@sheffield.ac.uk`

Abstract. High throughput technologies have increased the need for automated image analysis in a wide variety of microscopy techniques. Geometric active contour models provide a solution to automated image segmentation by incorporating statistical information in the detection of object boundaries. A statistical active contour may be defined by taking into account the optimisation of an information-theoretic measure between object and background. We focus on a product-type measure of divergence known as Cauchy-Schwartz distance which has numerical advantages over ratio-type measures. By using accurate shape derivation techniques, we define a new geometric active contour model for image segmentation combining Cauchy-Schwartz distance and Gabor energy texture filters. We demonstrate the versatility of this approach on images from the Brodatz dataset and phase-contrast microscopy images of cells.

Keywords: Geometric active contours · Cauchy-Schwartz distance · Gabor energy · Texture feature segmentation

1 Introduction

Due to high throughput technology, a great influx of imaging data has become available in biomedical research producing large datasets that need to be processed in a reliable and unbiased way. As a result, there is an increased need for computer automation throughout the imaging framework [1] and in particular in the extension from high throughput to assays that include dynamic behaviour over time [2]. Existing image analysis frameworks are focused either on pre-processing the image to remove artifacts and enhance signal-to-noise ratio [3]; or using local intensity and texture information to delineate the cell surface from the background [4]. The latter category is non technology-specific and coupled with the ability to estimate parameters from data has the potential to unify detection techniques [5].

Image segmentation is the task of partitioning an image into meaningful regions delineating objects and the background. Region-based segmentation takes into account the statistical properties of the image for example through density estimation techniques. Often the object regions are not Gaussian-distributed in pixel intensity making the detection by standard image analysis techniques (thresholding, edge-detection, region-based and connectivity preserving techniques) extremely challenging. This is the case in phase-contrast microscopy which is a widely used imaging technology, however images produced have low signal-to-noise ratio and illumination artifacts (bright halo around boundaries) caused by changes in object shape [3].

Active contour models are an unsupervised image segmentation technique consisting in defining a dynamic contour stretching over the object boundaries which partitions the image into distinct regions [6]. Geometric active contour models use an embedding of the contour into a higher dimensional surface (level set function) which is adapted to the information in the image until it converges to the object boundaries [7,8]. Geometric models overcome instability and topology problems of parametric active contours [6] and in addition enable probabilistic characterization of regions [9].

In this study, the Cauchy-Schwartz measure [10,11] of divergence is used to optimise image segmentation. Product-type measures such as Cauchy-Schwartz distance and Battacharyya distance [12] have numerical advantages over ratio-type measures including Kullback-Leibler [13] and Renyi's entropy in the approximation of region-specific distributions. By combining information theory, Gabor energy texture and a feature selection strategy, an automated segmentation strategy is described that can recover boundaries in textured images and challenging phase-contrast microscopy examples.

2 Materials and Methods

Let Ω_0 be a bounded open subset of \mathbb{R}^2 and let $I : \overline{\Omega}_0 \subset \mathbb{R}^2 \rightarrow \mathbb{R}$ represent an image. The partitioning of image Ω_0 into two non-overlapping regions: the target region Ω and the background region $\Omega_0 \setminus \Omega$ is defined by function $\mathbf{f} : \Omega_0 \subset \mathbb{R}^2 \rightarrow \mathbb{R}^n$, $\mathbf{f}(\mathbf{x}) = [f_1(\mathbf{x}), f_2(\mathbf{x}), \dots, f_n(\mathbf{x})]^T$ which associates any image location $\mathbf{x} = (x, y) \in \mathbb{R}^2$ to a vector of features f_i . The dimension of the feature space is determined by the nature of features, e.g. $n = 1$ for grayscale intensity, $n = 3$ for color images or large n in the case of texture.

Features observed over the target and background regions represent random variables independently sampled from a target distribution, $p_t(\mathbf{f}(\mathbf{x}))$ and a background distribution $p_b(\mathbf{f}(\mathbf{x}))$ defined as:

$$\begin{aligned} p_t(\mathbf{f}(\mathbf{x})) &= \frac{1}{||\Omega||} \int_{\Omega} K(\mathbf{f}(\mathbf{x}) - \mathbf{f}(\hat{\mathbf{x}})) d\hat{\mathbf{x}} \\ p_b(\mathbf{f}(\mathbf{x})) &= \frac{1}{||\Omega_0 \setminus \Omega||} \int_{\Omega_0 \setminus \Omega} K(\mathbf{f}(\mathbf{x}) - \mathbf{f}(\hat{\mathbf{x}})) d\hat{\mathbf{x}} \end{aligned} \quad (1)$$

where $\hat{\mathbf{x}}$ denote uniformly distributed sampling locations from where the feature observations $\mathbf{f}(\hat{\mathbf{x}})$ are collected and $K(\mathbf{f}(\mathbf{x}))$ is a Parzen (Gaussian) density estimation kernel [14].

In the following, the use of the Cauchy-Schwartz information-theoretic measure is discussed as basis for defining a new image segmentation model. Cauchy-Schwartz distance is a measure of divergence between two distributions. It is part of a class of cross-entropy measures that includes Kullback-Leibler, Battacharyya and Renyi's entropy. The Cauchy-Schwartz distance is derived from the Cauchy-Schwartz inequality [10]:

$$\|\mathbf{u}\|^2 \|\mathbf{v}\|^2 \leq (\mathbf{u}^T \mathbf{v})^2 \Leftrightarrow -\log \frac{\mathbf{u}^T \mathbf{v}}{\sqrt{\|\mathbf{u}\|^2 \|\mathbf{v}\|^2}} \geq 0. \quad (2)$$

where \mathbf{u} and \mathbf{v} are any two vectors. Cauchy-Schwartz distance is a product-type measure which alongside with Battacharyya distance has been shown to provide numerical advantages over ratio-type measures such as Kullback-Leibler in the approximation of region-specific distributions [11]. Given a partitioning of the image, region-specific p_t and p_b can be optimally estimated by modifying the partitioning in the direction of maximising Cauchy-Schwartz distance:

$$D_{CS}(p_t(\mathbf{f}(\mathbf{x})), p_b(\mathbf{f}(\mathbf{x}))) = -\log \frac{\int_{\mathbb{R}^n} p_t(\mathbf{f}(\mathbf{x})) p_b(\mathbf{f}(\mathbf{x})) d\mathbf{f}}{\sqrt{\int_{\mathbb{R}^n} p_b^2(\mathbf{f}(\mathbf{x})) d\mathbf{f} \int_{\mathbb{R}^n} p_t^2(\mathbf{f}(\mathbf{x})) d\mathbf{f}}} \geq 0. \quad (3)$$

2.1 Geometric Active Contour Model Based on Cauchy-Schwartz

The active contour partitioning of the image is represented using a level set function:

$$\Phi(\mathbf{x}) \begin{cases} > 0, & \text{if } \mathbf{x} \in \Omega \\ < 0, & \text{if } \mathbf{x} \in \Omega_0 \setminus \Omega \\ = 0, & \text{if } \mathbf{x} \in \partial\Omega \end{cases}. \quad (4)$$

Maximising (3) is equivalent to minimising the argument of the logarithm. In the following, this is referred to as the Cauchy-Schwartz (CS) criterion:

$$CS(p_t(\mathbf{f}(\mathbf{x})), p_b(\mathbf{f}(\mathbf{x}))) = \frac{\int_{\mathbb{R}^n} p_t(\mathbf{f}(\mathbf{x})) p_b(\mathbf{f}(\mathbf{x})) d\mathbf{f}}{\sqrt{\int_{\mathbb{R}^n} p_t^2(\mathbf{f}(\mathbf{x})) d\mathbf{f} \int_{\mathbb{R}^n} p_b^2(\mathbf{f}(\mathbf{x})) d\mathbf{f}}}. \quad (5)$$

Let the notations be introduced:

$$\begin{aligned} G_1(\mathbf{x}, \Omega) &= p_t(\mathbf{f}(\mathbf{x})); \quad G_3(\mathbf{x}, \Omega) = \int_{R^n} p_t^2(\mathbf{f}(\mathbf{x})) d\mathbf{f}; \\ G_2(\mathbf{x}, \Omega) &= p_b(\mathbf{f}(\mathbf{x})); \quad G_4(\mathbf{x}, \Omega) = \int_{R^n} p_b^2(\mathbf{f}(\mathbf{x})) d\mathbf{f}; \end{aligned} \quad (6)$$

We define the Cauchy-Schwartz region-based geometric active contour model as:

$$J(\Phi) = \int_{\mathbb{R}^n} \frac{G_1(\mathbf{x}, \Omega) G_2(\mathbf{x}, \Omega)}{\sqrt{G_3(\mathbf{x}, \Omega) G_4(\mathbf{x}, \Omega)}} d\mathbf{f} + \mu \int_{\partial\Omega} ds = J_1(\Phi) + J_2(\Phi) \quad (7)$$

where $J_1(\Phi)$ is a region-based term enforcing the CS criterion (5) and $J_2(\Phi)$ is a boundary-based term enforcing minimum length of the contour. The evolution of $\Phi(\mathbf{f}(\mathbf{x}), t)$ from an initial given state $\Phi(\mathbf{f}(\mathbf{x}), 0) = \Phi_0(\mathbf{f}(\mathbf{x}))$ in the direction of minimising (7) is parameterised by $t \geq 0$.

We use shape derivation theory [15, 16] to obtain the Euler derivative of (7). The term $J_1(\Phi) = \int_{R^n} k(\mathbf{x}, \Omega) d\mathbf{f}$ is a region-based term with region-dependent descriptor $k(\mathbf{x}, \Omega) = G_1(\mathbf{x}, \Omega)G_2(\mathbf{x}, \Omega)G_3(\mathbf{x}, \Omega)^{-1/2}G_4(\mathbf{x}, \Omega)^{-1/2}$. Derivation leads to a summation of region-based terms with region-dependent descriptors detailed in the Appendix. Therefore, the Euler derivative of J_1 in the direction of \mathbf{v} is:

$$dJ_{1r}(\Omega, \mathbf{v}) = \frac{A(\mathbf{x}, \Omega)}{\|\Omega_0 \setminus \Omega\|} \int_{\partial\Omega} \left(1 - \frac{G_2(\mathbf{x}, \Omega)}{G_4(\mathbf{x}, \Omega)}\right) G_1(\mathbf{x}, \Omega) * K(\mathbf{f}(\mathbf{x})) (\mathbf{v} \cdot \mathbf{n}) ds + \quad (8)$$

$$- \frac{A(\mathbf{x}, \Omega)}{\|\Omega\|} \int_{\partial\Omega} \left(1 - \frac{G_1(\mathbf{x}, \Omega)}{G_3(\mathbf{x}, \Omega)}\right) G_2(\mathbf{x}, \Omega) * K(\mathbf{f}(\mathbf{x})) (\mathbf{v} \cdot \mathbf{n}) ds$$

where $A(\mathbf{x}, \Omega) = G_3^{-1/2}(\mathbf{x}, \Omega)G_4^{-1/2}(\mathbf{x}, \Omega)$ and $*$ denotes convolution.

The term $J_2(\Phi)$ is a boundary-based term with boundary-independent descriptor, therefore $dJ_{2r}(\Omega, \mathbf{v}) = - \int_{\partial\Omega} \mu \operatorname{div} \left(\frac{|\nabla\Phi|}{\|\nabla\Phi\|} \right) (\mathbf{v} \cdot \mathbf{n}) ds$. The evolution equation becomes:

$$\frac{\partial\Phi}{\partial t} = \left[\frac{A(\mathbf{x}, \Omega)}{\|\Omega\|} \left(1 - \frac{G_1(\mathbf{x}, \Omega)}{G_3(\mathbf{x}, \Omega)}\right) (G_2(\mathbf{x}, \Omega) * K(\mathbf{f}(\mathbf{x}))) - \quad (9)$$

$$- \frac{A(\mathbf{x}, \Omega)}{\|\Omega_0 \setminus \Omega\|} \left(1 - \frac{G_2(\mathbf{x}, \Omega)}{G_4(\mathbf{x}, \Omega)}\right) (G_1(\mathbf{x}, \Omega) * K(\mathbf{f}(\mathbf{x}))) + \mu \operatorname{div} \left(\frac{|\nabla\Phi|}{\|\nabla\Phi\|} \right) \right] \mathbf{n}.$$

2.2 Gabor Energy Texture Features

Texture features include spatial information of pixel intensities. Commonly used in image processing is Gabor filtering which decomposes the image into sub-bands with a preferred orientation and spatial frequency by kernel convolution. The use of Gabor energy features sets the basis for a nonlinear multi-scale method of describing texture that resembles the way information is interpreted in the visual cortex [17, 18]. A 2D Gabor filter has the expression:

$$g_{\lambda, \sigma, \gamma, \theta, \varphi}(x, y) = e^{-\frac{x'^2 + \gamma^2 y'^2}{2\sigma^2}} \cos\left(2\pi \frac{x'}{\lambda} + \varphi\right) \quad (10)$$

$$x' = (x - x_0) \cos \theta + (y - y_0) \sin \theta$$

$$y' = -(x - x_0) \sin \theta + (y - y_0) \cos \theta$$

where $\theta \in [0 \pi)$ is the rotation angle of the gaussian envelope and λ and $\varphi \in (-\pi \pi]$ denote the spatial frequency and phase of the sinusoidal carrier. The Gaussian envelope is characterised by parameters γ , which specifies ellipticity and σ , a scaling parameter which controls the size of the Gaussian. The ratio σ/λ controls the number of parallel on and off stripes that the kernel contains.

This ratio is determined by the bandwidth b . In the following, we consider the case of $b = 1$ for which $\sigma = 0.56 \lambda$. The response of a Gabor filter (10) applied to an image is:

$$r_{\lambda,\sigma,\gamma,\theta,\varphi} = \int_{\Omega} I(u,v) g_{\lambda,\sigma,\gamma,\theta,\varphi}(x-u, y-v) du dv. \quad (11)$$

Gabor energy represents the combined magnitude of phase-shifted responses:

$$e_{\lambda,\sigma,\gamma,\theta}(x,y) = \sqrt{r_{\lambda,\sigma,\gamma,\theta,0}^2(x,y) + r_{\lambda,\sigma,\gamma,\theta,-\frac{\pi}{2}}^2(x,y)}. \quad (12)$$

Single Orientation Texture Features. Gabor energy feature function can be defined by discretising $\lambda = [\lambda_{min}, \lambda_{min} + \Delta\lambda, \dots]$, $\gamma = [\gamma_{min}, \gamma_{min} + \Delta\gamma, \dots]$ and $\theta = [\theta_1, \theta_2, \dots]$, $\theta_k = k \frac{\pi}{N}$, $k = 0, N-1$. Single orientation features are combined into a set:

$$\mathbf{f}^1 : \Omega_0 \in \mathbb{R}^n, \mathbf{f}^1(x,y) = [\mathbf{f}_{1,0}^1(x,y), \mathbf{f}_{1,1}^1(x,y) \dots \mathbf{f}_{n,N-1}^1(x,y)]^T \quad (13)$$

where $\mathbf{f}_{n,k}^1 = e_{\lambda_n, \gamma_n, \theta_k}(x,y)$.

Combined Orientation Texture Features. For textures without a preferred spatial orientation, combined Gabor energy features representing the superposition of Gabor energy terms for multiple orientations are added to a set:

$$\mathbf{f}^2 : \Omega_0 \in \mathbb{R}^n, \mathbf{f}^2(x,y) = [\mathbf{f}_1^2(x,y), \mathbf{f}_2^2(x,y) \dots \mathbf{f}_n^2(x,y)]^T \quad (14)$$

where $\mathbf{f}_n^2(x,y) = \sum_{k=1}^N e_{\lambda_n, \gamma_n, \theta_k}(x,y)$.

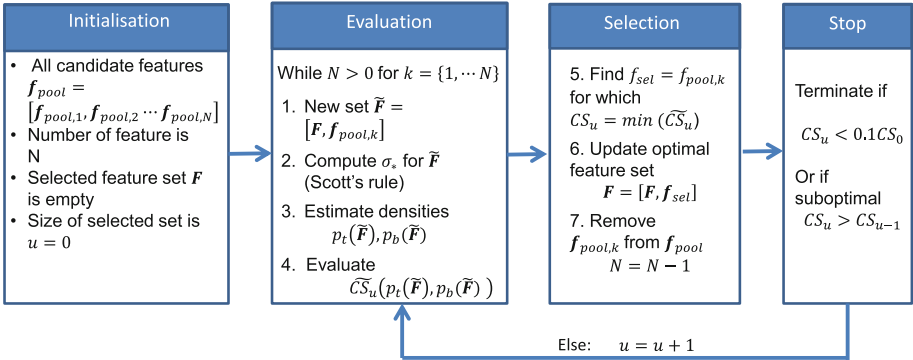


Fig. 1. Feature selection strategy produces a CS optimal feature set.

2.3 Feature Selection Strategy

The number of texture features increases computational complexity. This can be prevented by using a suitable feature selection strategy. In the following, a

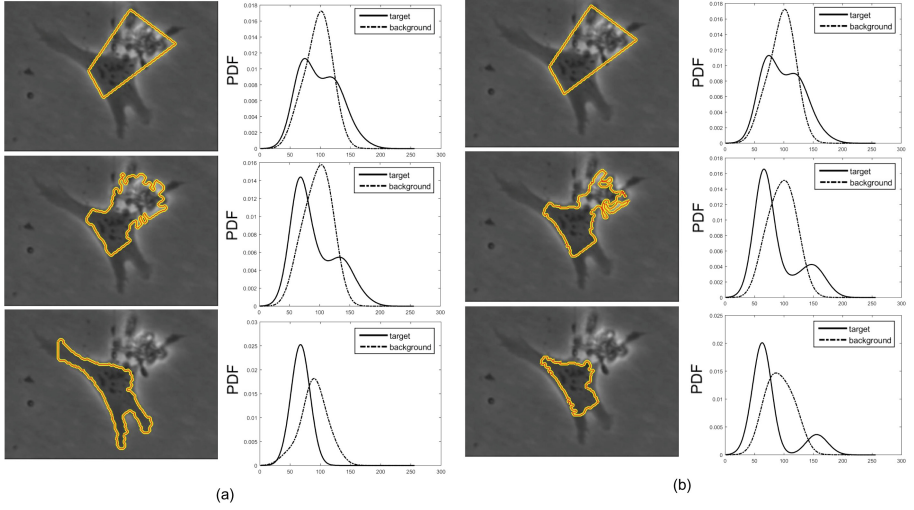


Fig. 2. Grayscale intensity segmentation using (a) Cauchy-Schwartz and (b) Kullback-Leibler models applied to a phase-contrast microscopy image of a cell: initialisation (top panel) is identical and evolution of the active contour is shown at intermediate (middle panel) and final (bottom panel) iterations accompanied by corresponding target and background distributions. Parameters $\mu = 0.001$; $w = 10$.

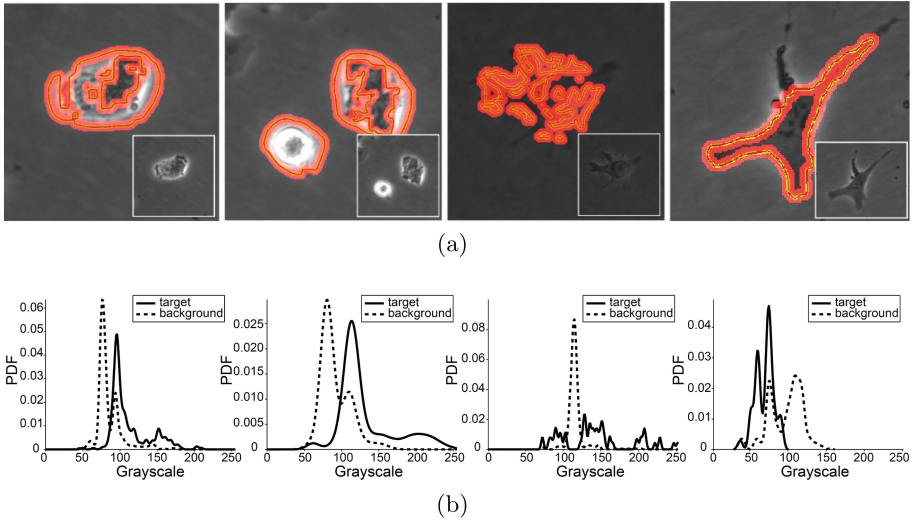


Fig. 3. Grayscale intensity segmentation using Cauchy-Schwartz model: (a) final iteration of active contour segmentation of phase-contrast microscopy images of cells (image inserts) with narrow band shown as a shaded region; (b) target and background distributions corresponding to contours in (a). Parameters $\mu = 0.2$; $w = 5$.

supervised approach is proposed to maximise the potential of each initialisation by using the region defined by Φ_0 as prior information of the densities of target p_t and the background p_b and performing selection based on the CS criterion (5). Given features $\mathbf{f}_{pool} = [\mathbf{f}_{pool,1}(x, y), \mathbf{f}_{pool,2}(x, y), \dots]$, procedure is detailed in Fig. 1.

The first feature, $\mathbf{f}_{pool,u,1}(x, y)$, is chosen according to the procedure: $\mathbf{f}_{sel,0}(x, y) = \mathbf{f}_{pool,1}(x, y)$ and the value of the criterion $CS_0(p_t, p_b)$ is used to evaluate the rest. Sequentially, features are added to a reduced feature set $\mathbf{F} = [\mathbf{f}_{sel,u}]$ and the potential of the selected set to discriminate between p_t and p_b is evaluated by optimising $CS_u(p_t(\mathbf{F}), p_b(\mathbf{F}))$. The feature selection strategy terminates when the criterion becomes worse $CS_u(p_t, p_b) > CS_{u-1}(p_t, p_b)$ or when it is sufficiently minimised $CS_u(p_t, p_b) < 0.1CS_0(p_t, p_b)$.

2.4 Numerical Implementation

The level set function Φ is initialised as a signed distance function and the pixels in the narrow-band region around the contour are updated followed by

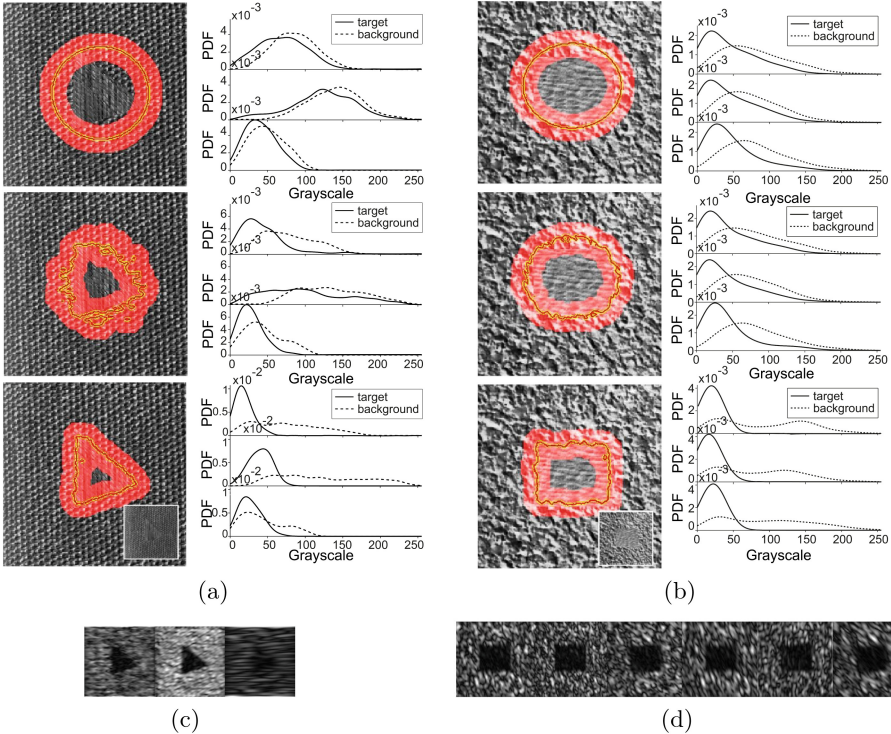


Fig. 4. Brodatz texture segmentation examples in images generated as fusion of two textures: (a, b) active contours evolving from initialisation (top), intermediate (middle) and final iteration (bottom) with corresponding estimated target and background distributions for three dominant features; (c) and (d) optimal feature sets corresponding to (a) and (b) respectively. Parameters $\mu = 0.2$, $w = 15$.

reinitialisation of the distance function to prevent numerical errors using the procedure in [19]. Density estimation was implemented using a (Parzen) Gaussian kernel with optimal variance obtained using Scott’s rule [14] where n and m represent number of features and pixels respectively: $\sigma_{\mathbf{X}}^2 = \frac{1}{n} \sum_{i=1}^n \sigma_{ii}^2$; $\sigma^* = \sigma_{\mathbf{X}} m^{\frac{1}{n+4}}$.

The narrow band technique was used to reduce computational complexity from $O(n^2)$ to $O(nk)$ where n and k represent the size of the image and of the narrow band region respectively [20]. Convergence was assessed from stationarity of the contour, i.e. less than 10% of pixels in the narrow band change sign in subsequent iterations. The geometric active contour parameters stiffness $\mu \in [0, 1]$ and width of the narrow band w are reported for each example.

3 Results

To demonstrate the ability of the Cauchy-Schwartz model to recover boundaries of objects, segmentation examples using grayscale are compared with an existing information theory-based active contour and limitations of using grayscale in phase-contrast microscopy images is discussed. Following this, Gabor energy texture segmentation is demonstrated on a number of Brodatz texture samples and phase-contrast microscopy images.

3.1 Segmentation of Phase-Contrast Images Based on Grayscale Intensity only Partially Recovers Boundaries

The CS-based geometric active contour was evaluated on images of cells acquired with a phase-contrast microscope (Fig. 2). Boundaries of the cell could be recovered in challenging examples where distributions of target and background regions showed significant overlap (Fig. 2a). We compared these results against a Kullback-Leibler (KL) active contour described in [13]. The KL model lead to faster convergence (Fig. 2b, 4 iterations) compared to CS (Fig. 2a, 11 iterations). Notably, cell debris was correctly excluded in the final contour by both models. However, by avoiding the local minimum in divergence visible in the final step of KL segmentation (Fig. 2b), the CS model recovered more of the object interior at the cost of increased number of iterations.

When applied to a wider phase-contrast microscopy image set results appeared mixed (Fig. 3) and boundaries were only partly recovered by the CS model (Fig. 3a) and no improvements were noted using KL (data not shown). Images with halo artifacts and the inclusion of dark and bright objects which are characteristic of phase-contrast, appeared to increase errors in the detection of target distributions (Fig. 3b). Overall, these examples indicated that not all microscopy images could be segmented using grayscale intensity alone. Given that the CS criterion showed increased detection compared to KL, we further tested the CS model by including information hidden in the texture characteristics of target and background regions.

3.2 Gabor Features Enable Detection of Noisy Object Boundaries in Textured Images

To investigate the ability to recover boundaries using Gabor texture features, test images were generated by fusing samples from the Brodatz [21] dataset (Fig. 4). The fused textures have similar mean intensity and contain noise thus resembling properties of microscopy images. A single orientation feature space was generated using $b = 1$, $\lambda = [1/15, 1/30, 1/60, 1/120, 1/240]$, $\gamma = [0.2, 0.4, 0.6, 0.8, 1]$; this was reduced to an optimal feature set using the CS-based feature selection strategy and the active contour was able to successfully recover the boundaries by estimating the target and background distributions. More features are selected in the example (Fig. 4b) and they appear more similar to each other when compared to (Fig. 4c). This suggested that a sparse feature set may be preferable to a finely sampled one.

3.3 Cauchy-Schwartz Model Detects Cells in Phase-Contrast Images Using Gabor Features

The performance of the geometric active contour and feature selection strategy were tested on real microscopy images displaying cells with bright and dark cell interior (Figs. 5 and 6). The texture of cells has no preferred orientation, therefore the feature space was combined from features at 8 different orientations followed by reduction to an optimal feature set. The active contour could detect each cell separately (Fig. 5) as well as jointly (Fig. 6). As expected, initial CS level exceeded the optimal threshold (final CS_u) obtained by the feature selections strategy (Fig. 1) but consistently fell under at large iteration numbers in all examples (Figs. 5c, d and 6b; dashed lines indicate optimal threshold). Boundaries of the dark cell (Fig. 5a) were easiest to detect as indicated by a large drop followed by approximately linear decay in the evolution of CS criterion (Fig. 5c). The bright cell example (Fig. 5b) posed increased difficulty in detection thus requiring larger iteration numbers compared to the dark one. In this case, the trend of the CS criterion showed a region of local minima followed by slow exponential decay (Fig. 5d). The combined bright and dark cell segmentation (Fig. 6a) proved the most challenging with multiple local minima and requiring the most iterations to achieve minimisation below the optimal threshold (Fig. 6b). These examples highlight that the problem of simultaneous segmentation of multiple objects with different intensity characteristics has an unexpectedly high level of difficulty when compared to the detection of individual objects. Nevertheless, the proposed feature selection and CS-based segmentation strategy is flexible enough to deal with either case and thus provides a solid basis for multiple object detection in microscopy images.

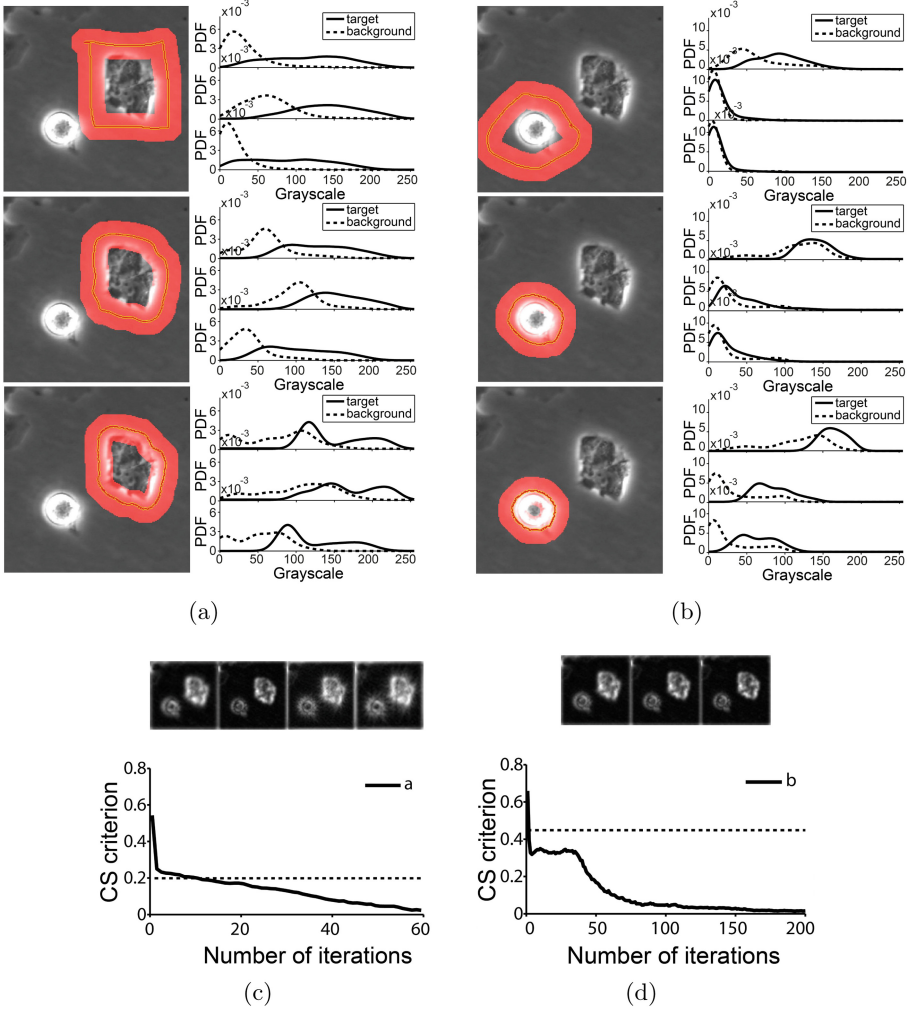


Fig. 5. Single cell detection using texture: (a, b) active contours evolving from initialisation (top), intermediate (middle) and final (bottom) iterations applied to a cell with (a) dark and (b) bright cell interior; (c) and (d) show optimal features and criterion minimisation corresponding to (a) and (b) respectively. Parameters $\mu = 0.2$; $w = 15$.

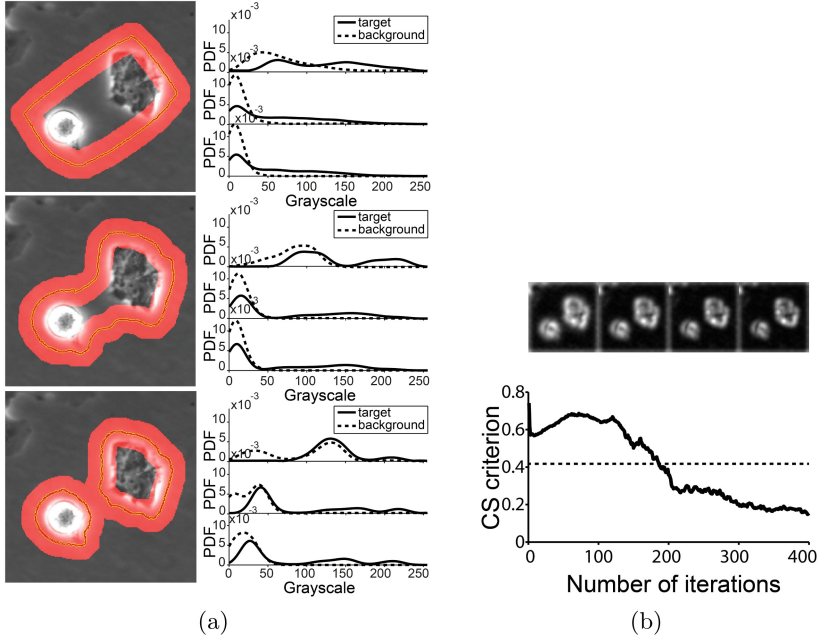


Fig. 6. Multiple cell detection using texture shows natural splitting of the contour to recover individual target regions: (a) active contours evolving from initialisation (top), intermediate (middle) and final (bottom) iterations applied to a phase-contrast microscopy image of cells with bright and dark cell interior; (b) optimal feature sets and minimisation of criterion corresponding to (a); dashed line indicates optimal values of criterion predicted by the feature selection strategy. Parameters $\mu = 0.2$; $w = 15$.

4 Conclusions

The challenges of segmentation in phase-contrast microscopy images were addressed through a strategy combining information theory and Gabor energy features. A new image segmentation model was defined to optimise Cauchy-Schwartz (CS) distance between a desired (target) region and the background using a geometric active contour model. The CS model incorporates the use of a product-type measure of divergence and shape derivation techniques contributing to improved numerical accuracy. Similar to CS, segmentation based on Battacharyya distance was shown to improve detection compared to ratio-type measures [12]. Indeed in grayscale only segmentation, the CS model produced better separation between target and background regions in phase-contrast image of cells when compared to a Kullback-Leibler (KL) model [13] but at the cost of lower convergence speed. However, these results were confined to a subset of images exhibiting relatively smooth dark cell interior and boundaries of cells with mixed bright and dark appearance and halo artifacts failed to be detected by either CS or KL.

Texture information based on Gabor energy critically improved the recovery of boundaries of objects (either artificially generated or microscopic cells) with various intensity distributions. By incorporating Gabor energy features into the CS model, textured objects with geometric orientation could be recovered with single orientation features while microscopy images of cells which have non specific orientation required combined orientation texture features. The introduction of texture information posed the problem of increased computational complexity which was solved through a CS-specific feature selection strategy to ensure optimal segmentation.

Overall, this study introduces a unified approach to achieve active contour segmentation based on the Cauchy-Schwartz information theoretic measure. By the inclusion of unsupervised feature learning from training target and background datasets, this work could enable general detection of target objects without prior information of intensity distribution characteristics of the image. By extension to tracking it could address the lack of a generic platform for detection of multiple regions in biological images which is a major setback in the automation of high throughput analysis including dynamic behaviour over time.

Acknowledgments. VB was funded by a doctoral scholarship from The University of Sheffield. Authors kindly thank members of the Peter W Andrews Laboratory at the Centre for Stem Cell Biology for providing the microscopy images of cells.

Appendix

The derivative of J_1 in the direction of \mathbf{v} is computed as:

$$dJ_{1r}(\Omega, \mathbf{v}) = \int_{R^n} k_s(\mathbf{x}, \Omega, \mathbf{v}) d\mathbf{f} - \int_{\partial\Omega} k(\mathbf{x}, \Omega)(\mathbf{v} \cdot \mathbf{n}) ds \quad (15)$$

The shape derivative of k in the direction of \mathbf{v} is given by:

$$k_s(\Omega, \mathbf{v}) = \frac{\partial k}{\partial G_1} dG_{1r}(\Omega, \mathbf{v}) + \frac{\partial k}{\partial G_2} dG_{2r}(\Omega, \mathbf{v}) + \frac{\partial k}{\partial G_3} dG_{3r}(\Omega, \mathbf{v}) + \frac{\partial k}{\partial G_4} dG_{4r}(\Omega, \mathbf{v}). \quad (16)$$

The term G_1 is a region-based term with region-dependent descriptor.

$$G_1(\mathbf{x}, \Omega) = \int_{\Omega} H_1(\mathbf{x}, \Omega) d\hat{\mathbf{x}}; \quad H_1(\mathbf{x}, \Omega) = \frac{K(\mathbf{f}(\mathbf{x}) - \mathbf{f}(\hat{\mathbf{x}}))}{K_{11}(\mathbf{x}, \Omega)}; \quad (17)$$

$$K_{11}(\mathbf{x}, \Omega) = \int_{\Omega} L_{11}(\mathbf{x}, \Omega) d\hat{\mathbf{x}}; \quad L_{11}(\mathbf{x}, \Omega) = 1.$$

The Eulerian derivative of G_1 is:

$$dG_{1r}(\mathbf{x}, \Omega, \mathbf{v}) = \frac{1}{\|\Omega\|} \int_{\partial\Omega} (p_t(\mathbf{f}(\mathbf{x})) - K(\mathbf{f}(\mathbf{x}) - \mathbf{f}(s))) (\mathbf{v} \cdot \mathbf{n}) ds. \quad (18)$$

Similarly, the derivative of G_2 is:

$$dG_{2r}(\mathbf{x}, \Omega_0 \setminus \Omega, \mathbf{v}) = -\frac{1}{\|\Omega_0 \setminus \Omega\|} \int_{\partial\Omega} (p_b(\mathbf{f}(\mathbf{x})) - K(\mathbf{f}(\mathbf{x}) - \mathbf{f}(s))) (\mathbf{v} \cdot \mathbf{n}) ds. \quad (19)$$

Note that the expression (19) has a change of sign due to the normal vector \mathbf{n} that changes direction w.r.t. the target and background region.

The term G_3 is a function of region-based terms:

$$G_3(\mathbf{x}, \Omega, \mathbf{v}) = \int_{R^n} H_3(\mathbf{x}, \Omega) d\mathbf{f}; \quad H_3(\mathbf{x}, \Omega) = \frac{K_{31}(\mathbf{x}, \Omega)^2}{K_{32}(\mathbf{x}, \Omega)^2}. \quad (20)$$

The shape derivative of H_3 in the direction \mathbf{v} of (20) is:

$$H_{3s}(\Omega, \mathbf{v}) = \frac{\partial H_3}{\partial K_{31}} dK_{31r} + \frac{\partial H_3}{\partial K_{32}} dK_{32r} \quad (21)$$

where the terms K_{31} , K_{32} are region-dependent terms with region-dependent descriptors and factorise as:

$$\begin{aligned} K_{31}(\mathbf{x}, \Omega) &= \int_{\Omega} L_{31}(\mathbf{x}, \Omega) d\hat{\mathbf{x}}; \quad L_{31}(\mathbf{x}, \Omega) = K(\mathbf{f}(\mathbf{x}) - \mathbf{f}(\hat{\mathbf{x}})); \\ K_{32}(\mathbf{x}, \Omega) &= \int_{\Omega} L_{32}(\mathbf{x}, \Omega) d\hat{\mathbf{x}}; \quad L_{32}(\mathbf{x}, \Omega) = 1. \end{aligned} \quad (22)$$

The corresponding derivatives are:

$$\begin{aligned} dK_{31r} &= - \int_{\partial\Omega} K(\mathbf{f}(\mathbf{x}) - \mathbf{f}(\hat{\mathbf{x}})) (\mathbf{v} \cdot \mathbf{n}) ds \\ dK_{32r} &= - \int_{\partial\Omega} (\mathbf{v} \cdot \mathbf{n}) ds. \end{aligned} \quad (23)$$

Substituting (23) into (21), the expression for the derivative of G_3 becomes:

$$dG_{3r}(\mathbf{x}, \Omega, \mathbf{v}) = \frac{2}{\|\Omega\|} \int_{\partial\Omega} (G_3(\mathbf{x}, \Omega) - K(\mathbf{f}(\mathbf{x}) - \mathbf{f}(\hat{\mathbf{x}}))) (\mathbf{v} \cdot \mathbf{n}) ds. \quad (24)$$

Similarly, the derivation of the term G_4 with a sign change corresponding to the orientation of \mathbf{n} w.r.t. the background region has the expression:

$$dG_{4r}(\mathbf{x}, \Omega_0 \setminus \Omega, \mathbf{v}) = -\frac{2}{\|\Omega_0 \setminus \Omega\|} \int_{\partial\Omega} (G_4(\mathbf{x}, \Omega) - K(\mathbf{f}(\mathbf{x}) - \mathbf{f}(\hat{\mathbf{x}}))) (\mathbf{v} \cdot \mathbf{n}) ds. \quad (25)$$

Substituting results (18), (19), (24), (25) into (16), the shape derivative of the descriptor k is obtained:

$$\begin{aligned} k_s(\Omega, \mathbf{v}) &= \frac{1}{\|\Omega\|} \int_{\partial\Omega} G_2 G_3^{-1/2} G_4^{-1/2} (G_1 - K) (\mathbf{v} \cdot \mathbf{n}) ds \\ &\quad - \frac{1}{\|\Omega_0 \setminus \Omega\|} \int_{\partial\Omega} G_1 G_3^{-1/2} G_4^{-1/2} (G_2 - K) (\mathbf{v} \cdot \mathbf{n}) ds \\ &\quad - \frac{1}{\|\Omega\|} \int_{\partial\Omega} G_1 G_2 G_3^{-3/2} G_4^{-1/2} (G_3 - K) (\mathbf{v} \cdot \mathbf{n}) ds \\ &\quad + \frac{1}{\|\Omega_0 \setminus \Omega\|} \int_{\partial\Omega} G_1 G_2 G_3^{-1/2} G_4^{-3/2} (G_4 - K) (\mathbf{v} \cdot \mathbf{n}) ds. \end{aligned} \quad (26)$$

Following cancellation of duplicate terms and reordering, the final expression for the Eulerian derivative of criterion term J_1 is obtained:

$$\begin{aligned}
 dJ_{1r}(\Omega, \mathbf{v}) = & -\frac{A(\mathbf{x}, \Omega)}{\|\Omega\|} \int_{\partial\Omega} \left(1 - \frac{G_1(\mathbf{x}, \Omega)}{G_3(\mathbf{x}, \Omega)}\right) \\
 & \int_{\mathbb{R}^n} G_2(\mathbf{x}, \Omega) K(\mathbf{f}(\mathbf{x}) - \mathbf{f}(\hat{\mathbf{x}})) d\mathbf{f}(\mathbf{v} \cdot \mathbf{n}) ds \\
 & + \frac{A(\mathbf{x}, \Omega)}{\|\Omega_0 \setminus \Omega\|} \int_{\partial\Omega} \left(1 - \frac{G_2(\mathbf{x}, \Omega)}{G_4(\mathbf{x}, \Omega)}\right) \\
 & \int_{\mathbb{R}^n} G_1(\mathbf{x}, \Omega) K(\mathbf{f}(\mathbf{x}) - \mathbf{f}(\hat{\mathbf{x}})) d\mathbf{f}(\mathbf{v} \cdot \mathbf{n}) ds
 \end{aligned} \tag{27}$$

where $A(\mathbf{x}, \Omega) = G_3^{-1/2}(\mathbf{x}, \Omega) G_4^{-1/2}(\mathbf{x}, \Omega)$.

References

1. Eliceiri, K.W., Berthold, M.R., Goldberg, I.G., et al.: Biological imaging software tools. *Nat. Methods* **9**(7), 697–710 (2012)
2. Allison, T.F., Powles-Glover, N.S., Biga, V., Andrews, P.W., Barbaric, I.: Human pluripotent stem cells as tools for high-throughput and high-content screening in drug discovery. *Int. J. High Throughput Screen.* **5**, 1–13 (2015)
3. Yin, Z., Kanade, T., Xu, D., Fisher, J.: Understanding the phase contrast optics to restore artifact-free microscopy images for segmentation. *Med. Image Anal.* **16**(5), 1047–1062 (2012)
4. Dewan, M.A., Ahmad, M.O., Swamy, M.N.: A method for automatic segmentation of nuclei in phase-contrast images based on intensity, convexity and texture. *IEEE Trans. Biomed. Circuits Syst.* **8**(5), 716–728 (2014)
5. Held, C., Palmisano, R., Haberle, L., et al.: Comparison of parameter-adapted segmentation methods for fluorescence micrographs. *Cytometry A* **79**(11), 933–945 (2011)
6. Blake, A., Zisserman, A.: *Visual Reconstruction*. MIT Press, Cambridge (1987)
7. Caselles, V., Catte, F., Coll, T., et al.: A geometric model for active contours in image processing. *Numerische Mathematik* **66**, 1–31 (1993)
8. Malladi, R., Sethian, J.A., Vemuri, B.C.: Shape modeling with front propagation: a level set approach. *IEEE Trans. Pattern Anal. Mach. Intell.* **17**, 158–175 (1995)
9. Cremers, D., Rousson, M., Deriche, R.: A review of statistical approaches to level set segmentation. *Int. J. Comput. Vis.* **72**, 195–215 (2007)
10. Principe, J., Xu, D., Fisher, J.: information theoretic learning. In: *Unsupervised Adaptive Filtering*. Wiley, New York (2000)
11. Gokcay, E., Principe, J.C.: Information theoretic clustering. *IEEE Trans. Pattern Anal. Mach. Intell.* **24**(2), 158–171 (2002)
12. Michailovich, O.V., Rath, Y., Tannenbaum, A.: Image segmentation using active contours driven by the Battacharya gradient flow. *IEEE Trans. Image Process.* **16**(11), 2787–2801 (2007)
13. Houhou, N., Thiran, J.P., Bresson, X.: Fast texture segmentation model based on the shape operator and active contour. *Proc. IEEE Comput. Vis. Pattern Recognit.* **53**, 1–8 (2008)

14. Scott, D.W.: *Multivariate Density Estimation: Theory, Practice and Visualisation*. Probability and Statistics. Wiley, New York (1992)
15. Jehan-Besson, S., Barlaud, M., Aubert, G.: Video object segmentation using Eulerian region-based active contours. In: *International Conference on Computer Vision*, pp. 353–361 (2001)
16. Aubert, G., Barlaud, M., Faugeras, O., et al.: Image segmentation using active contours: calculus of variations or shape gradients. *SIAM J. Appl. Math.* **63**, 2128–2154 (2002)
17. Petkov, N., Kruizinga, P.: Computational models of visual neurons specialised in the detection of periodic and aperiodic visual stimuli: bar and grating cells. *Biol. Cybern.* **76**(2), 83–96 (1997)
18. Kruizinga, P., Petkov, N.: Nonlinear operator for oriented texture. *IEEE Trans. Image Process.* **8**, 1395–1407 (1999)
19. Sussman, M., Smerenca, P., Osher, S.J.: A level set approach for computing solutions to incompressible two-phase flow. *J. Comput. Phys.* **114**, 146–159 (1994)
20. Adalsteinsson, D., Sethian, J.: A fast level set method for propagating interfaces. *J. Comput. Phys.* **118**, 269–277 (1995)
21. <http://www.ux.uis.no/~tranden/brodatz.html>

Computational Intelligence Methods for Bioinformatics
and Biostatistics

13th International Meeting, CIBB 2016, Stirling, UK,

September 1-3, 2016, Revised Selected Papers

Bracciali, A.; Caravagna, G.; Gilbert, D.; Tagliaferri, R.

(Eds.)

2017, XXII, 249 p. 98 illus., Softcover

ISBN: 978-3-319-67833-7